metals

MDPI

Article

Production and Characterization of a 316L Stainless Steel/β-TCP Biocomposite Using the Functionally Graded Materials (FGMs) Technique for Dental and Orthopedic Applications

Bruna Horta Bastos Kuffner [1], Patricia Capellato [2,*], Larissa Mayra Silva Ribeiro [2], Daniela Sachs [2] and Gilbert Silva [1]

[1] Institute of Mechanical Engineering, Unifei—Federal University of Itajubá. Av. BPS, 1303, Itajubá 37500-903, Brazil; brunakuffner@hotmail.com (B.H.B.K.); gilbert@unifei.edu.br (G.S.)
[2] Institute of Physics and Chemistry, Unifei—Federal University of Itajubá. Av. BPS, 1303, Itajubá 37500-903, Brazil; larissamayra@unifei.edu.br (L.M.S.R.); danisachs@unifei.edu.br (D.S.)
* Correspondence: capellato@unifei.edu.br; Tel.: +55-129-9713-2674

Abstract: Metallic biomaterials are widely used for implants and dental and orthopedic applications due to their good mechanical properties. Among all these materials, 316L stainless steel has gained special attention, because of its good characteristics as an implantable biomaterial. However, the Young's modulus of this metal is much higher than that of human bone (~193 GPa compared to 5–30 GPa). Thus, a stress shielding effect can occur, leading the implant to fail. In addition, due to this difference, the bond between implant and surrounding tissue is weak. Already, calcium phosphate ceramics, such as beta-tricalcium phosphate, have shown excellent osteoconductive and osteoinductive properties. However, they present low mechanical strength. For this reason, this study aimed to combine 316L stainless steel with the beta-tricalcium phosphate ceramic (β-TCP), with the objective of improving the steel's biological performance and the ceramic's mechanical strength. The 316L stainless steel/β-TCP biocomposites were produced using powder metallurgy and functionally graded materials (FGMs) techniques. Initially, β-TCP was obtained by solid-state reaction using powders of calcium carbonate and calcium phosphate. The forerunner materials were analyzed microstructurally. Pure 316L stainless steel and β-TCP were individually submitted to temperature tests (1000 and 1100 °C) to determine the best condition. Blended compositions used to obtain the FGMs were defined as 20% to 20%. They were homogenized in a high-energy ball mill, uniaxially pressed, sintered and analyzed microstructurally and mechanically. The results indicated that 1100 °C/2 h was the best sintering condition, for both 316L stainless steel and β-TCP. For all individual compositions and the FGM composite, the parameters used for pressing and sintering were appropriate to produce samples with good microstructural and mechanical properties. Wettability and hemocompatibility were also achieved efficiently, with no presence of contaminants. All results indicated that the production of 316L stainless steel/β-TCP FGMs through PM is viable for dental and orthopedic purposes.

Keywords: 316L stainless steel; beta-tricalcium phosphate; biomaterials; powder metallurgy; functionally graded materials

check for updates

Citation: Kuffner, B.H.B.; Capellato, P.; Ribeiro, L.M.S.; Sachs, D.; Silva, G. Production and Characterization of a 316L Stainless Steel/β-TCP Biocomposite Using the Functionally Graded Materials (FGMs) Technique for Dental and Orthopedic Applications. *Metals* **2021**, *11*, 1923. https://doi.org/10.3390/met11121923

Academic Editors: Yadir Torres Hernández and Asit Kumar Gain

Received: 15 October 2021
Accepted: 23 November 2021
Published: 29 November 2021

Publisher's Note: MDPI stays neutral with regard to jurisdictional claims in published maps and institutional affiliations.

Copyright: © 2021 by the authors. Licensee MDPI, Basel, Switzerland. This article is an open access article distributed under the terms and conditions of the Creative Commons Attribution (CC BY) license (https://creativecommons.org/licenses/by/4.0/).

1. Introduction

Biomaterials compose a wide range of materials of various types, including alloys, ceramics, glasses and biodegradable and non-degradable polymers, among others. They are used in different areas of medicine and dentistry, for the repair or replacement of damaged body parts. To be considered biocompatible and avoid compromising the patient's health, the material must not induce cytotoxic reactions in the organism [1,2]. The biomaterials market is growing expansively, and according to the compound annual growth rate, it is estimated that in five years the numbers can vary from 5.5% to 32% in some areas [3].

Metallic biomaterials are widely used for clinical applications, representing about 70% of all medical devices manufactured in the world, due to their good durability and excellent mechanical properties [4].

The most common metallic materials used in the fabrication of these components include pure titanium, titanium–aluminum–vanadium, cobalt–chromium alloys and stainless steels. They are often used because of their optimum load-bearing characteristics, high ductility, wear and corrosion resistance. In the last decades, stainless steel has been considered the main metal used for permanent [5,6] and non-permanent implant applications [4] such as bone plates, pins and screws. This is because of its efficient biocompatibility, corrosion resistivity and low cost when compared to titanium, cobalt and vanadium alloys [7,8]. However, metallic implants have a limitation due to their Young's modulus. Cortical bone presents a Young's modulus value between 5 and 30 GPa, while, for 316L stainless steel, it is about 190 GPa [9,10]. This difference can lead the implant to instability and failure due to the stress shielding effect, which causes non-union between implant and bone, bone necrosis and delay in the healing process [11].

In order to improve 316L stainless steel's performance, various techniques have been studied, from those focused on the coating surface to improve biocompatibility and minimize the corrosion rate [11] to the use of drugs, to protect the material surface from the corrosive physiological environment [12]. Furthermore, the association of this steel with a bioceramic was analyzed to enhance their individual properties, for use as a composite biomaterial for dental and orthopedic purposes, as seen in this research.

Calcium phosphate constitutes about 60 wt.% of bone, being the major inorganic material of the bone system and representing 90 wt.% of the enamel tooth [12]. For this reason, calcium-phosphate-based ceramics, especially beta-tricalcium phosphate (β-TCP), are often used to replace small areas of the body, such as facial and dental traumas. In addition, calcium phosphate present in the bone structure is responsible for the bone-healing process, due to the osteoinductive aspect [12]. This fact is directly related to the chemical composition of β-TCP, which is very close to the mineral phase of the bone.

Previous studies indicate that β-TCP provides attachment, differentiation and proliferation of osteoblasts and mesenchymal cells [13,14]. Moreover, the Young's modulus of β-TCP is similar to that of the bone, which makes them both work together under mechanical stress. The main disadvantages of this ceramic include its low mechanical strength, which precludes its use in large areas of the body [15,16] and its high resorption speed when compared to natural bone [17]. However, in terms of resorption, β-TCP can be better than other bioceramics such as hydroxyapatite (HAp). HAp has low properties of resorption, inducing fractures inside the material or deficiency in the bond between the interface of the bone and implant, resulting in bone deformation over the years. Furthermore, HAp residue can injure the intrinsic strength of bone [18].

Powder metallurgy is a route widely used to produce workpieces through pressing and sintering steps, using powders as precursor materials. With this, it is possible to obtain materials with specific chemical compositions and shapes that are difficult to achieve by conventional casting processes (as in the case of elements with high melting points, such as tungsten, tantalum and niobium). Furthermore, there is no waste production, which makes this process cleaner for the environment than other processes [19,20].

Functionally graded materials (FGMs) have been investigated since the 1980s. In this technique, materials are manufactured by powder metallurgy but compacted differently, forming a composite with different materials and adapting its microstructure through the composite phases [21]. Instead of the usual pressing in single composition, the workpiece is pressed by overlapping several small layers, or gradients, varying the composition and microstructure continuously. In each of these layers, the properties are differentiated, as each material has specific mechanical, chemical, physical and microstructural characteristics [22]. For this reason, FGMs can be considered multiphase, and their manufacturing process, as well as the material composition, influences the phases formed [21]. Initially, FGMs were developed to solve thermal problems in space shuttles. However, researchers

found that this route was extremely interesting for the production biomaterials since the functional gradient simulates the natural condition of human bone [9,22].

Thus, this study aimed to obtain a biocomposite that combines the excellent mechanical properties of 316L stainless steel with the excellent osteoinduction and osteoconduction of β-TCP, by combining powder metallurgy with functional gradation. Thereby, it is possible to create a final product for dental and orthopedic applications.

2. Materials and Methods

To produce 316L/β-TCP composites, 316L stainless steel was obtained from Höganäs® (Hoganas, Sweden), as gas atomized powder, with spherical morphology (Figure 1a) and an average particle size of 46 µm (Figure 1b). The chemical composition of 316L stainless steel can be seen in Table 1, according to the Höganäs datasheet [23].

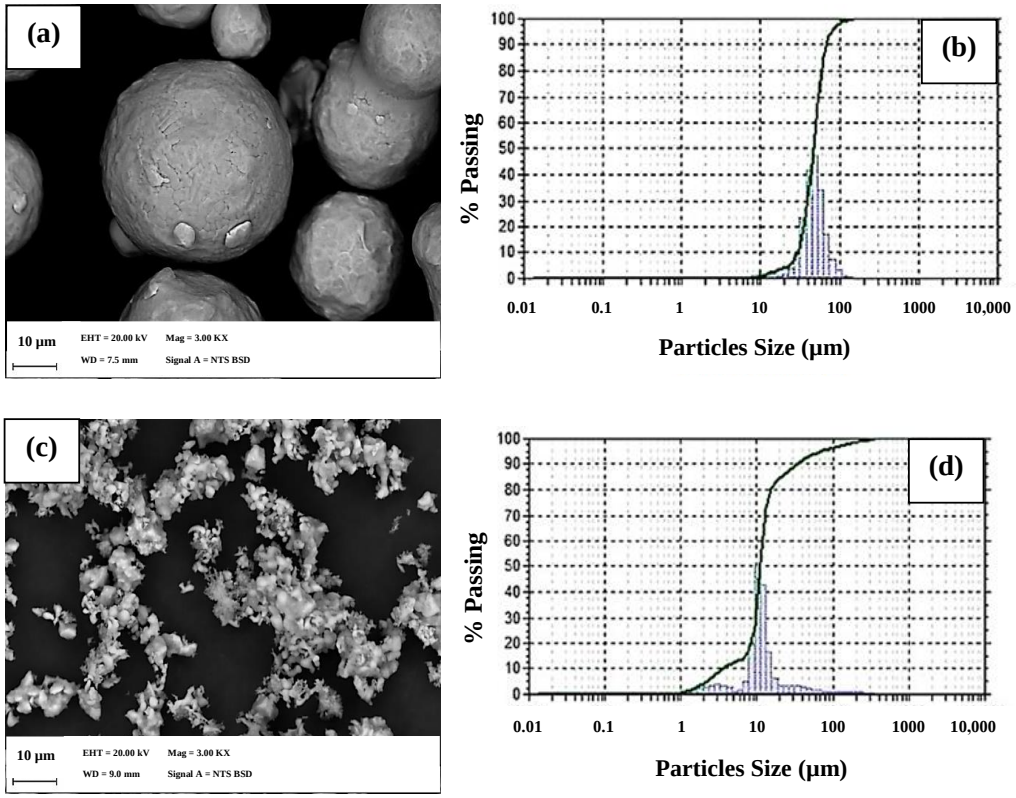


Figure 1. Particles size via SEM. (**a**) 316L stainless steel and (**c**) β-TCP and laser granulometry; (**b**) 316L stainless steel and (**d**) β-TCP.

Table 1. 316L stainless steel chemical composition.

Chemical Element	Content %
Cr	17
Ni	12
Mo	2.5
Mn	1.5
Si	0.8
C	0.01
O	0.06
N	0.10
Fe	Balance

β-TCP was obtained as in [24], using calcium carbonate ($CaCO_3$) and calcium phosphate ($CaHPO_4$) reagents as powders, according to Equation (1):

$$CaCO_{3(s)} + 2CaHPO_{4(s)} \rightarrow Ca_3(PO_4)_{2(s)} + H_2O_{(g)} + CO_{2(g)} \quad (1)$$

The powders were inserted in a mixer of the Edibon, model V-Blender (Edibon LTD, Leganés, Madrid, Spain) with a speed of 18 rpm for 2 h. After this process, they were dried at 100 °C for 1 h and sintered in an oven of the EDG Equipments and Controls, model EDG 3P-S (EDG Equipment LTD, São Carlos, Brazil) for 6 h at 1050 °C, with a heating rate of 10 °C/min. The powders' deagglomeration was performed using a high-energy ball mill of the Noah Nuoya, model NQM 0.2 L (Yangzhou Nuoya Machinery CO., LTD, Yangzhou, Hanjiang District, China) for 1 h, at 150 rpm of milling speed and ball to powder ratio of 10:1. The particles obtained presented irregular morphology, as seen in Figure 2a, and an average particle size of 10–12 µm, represented in Figure 2b.

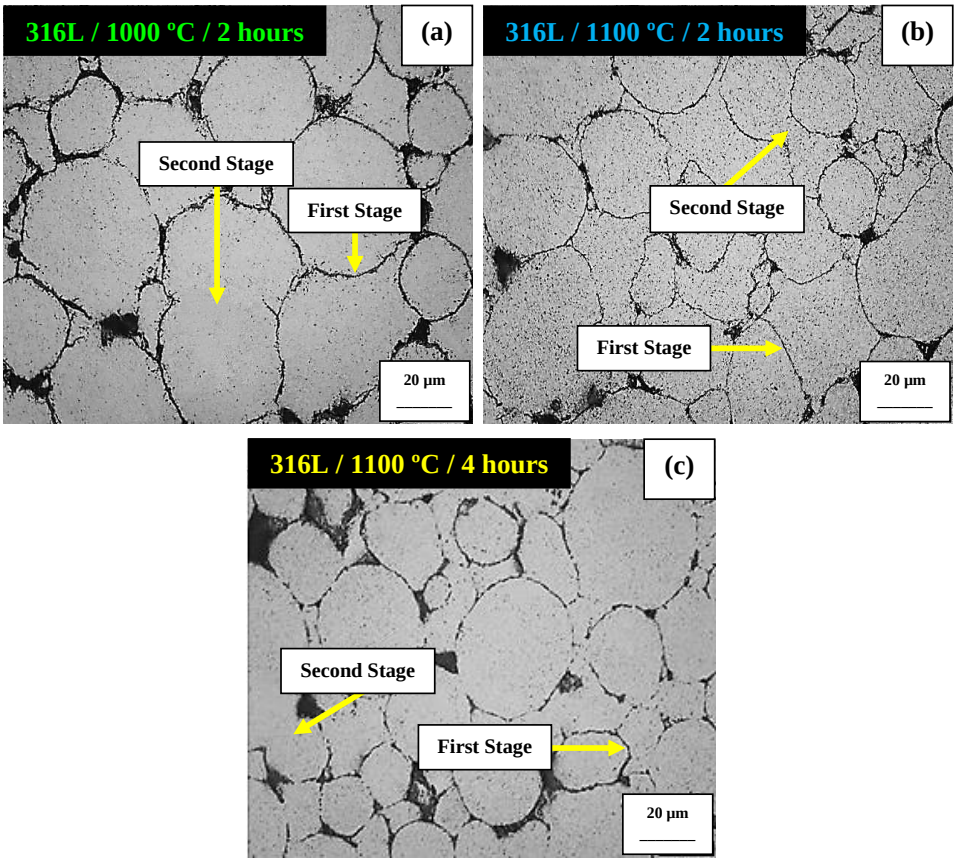


Figure 2. The 316L stainless steel sintered at (**a**) 1000 °C for 2 h, (**b**) 1100 °C for 2 h, and (**c**) 1100 °C for 4 h.

The small granulometry observed in β-TCP particles deagglomerated in a high-energy ball mill leads to the formation of clusters. It happens because of the tendency of very fine powders to agglomerate, due to their extremely high surface energy and unsaturation. Thus, the particles join together to achieve balance [25].

The individual layers of FGM require a composition evaluation. In this study, the upper layers had a higher concentration of 316L stainless steel, which decreased with a successive increase of β-TCP in the composition of the bottom layers. Healing bone fractures requires a precise alignment with a minimum motion of the bone in situ [26]. However, metallic devices used for these purposes have some disadvantages related to their Young's modulus, which is much higher than that of natural bone [9]. Therefore, FGM composites were produced to overcome these disadvantages, due to their ability to

imitate the natural gradation seen in bone tissue. In addition, knowing that the design of the implant can directly affect fracture healing, FGMs are considered interesting, since that they can provide a bending stiffness, while their Young's modulus remains close to the bone's Young's modulus, avoiding stress shielding effect [11,27]. In addition, FGMs provide morphological properties that lead to good mechanical and physical characteristics due to the related parameter control [9].

In this research, the FGM gradient was defined by varying the 316L stainless steel and β-TCP contents by 20% per layer, completing six different compositions as seen in Table 2. The layers were defined according to an extensive study of literature [28–32]. The 316L stainless steel was blended with β-TCP using a high-energy ball mill for 1 h, with a speed of 150 rpm and a ball to powder ratio of 10:1. This process was performed in an inert, N5-grade argon atmosphere (99.999%).

Table 2. Composition of FGM layers.

Layer	Composition	Constitution (*v*/*v*%)
1	Pure	100% 316L
2	Blended	80% 316L–20% β-TCP
3	Blended	60% 316L–40% β-TCP
4	Blended	40% 316L–60% β-TCP
5	Blended	20% 316L–80% β-TCP
6	Pure	100% β-TCP

To produce the FGM composite, each layer with 1.3 mm of thickness was inserted on top of another, in a 9 mm of diameter metallic matrix. After this, the FGM was compacted in a uniaxial press (Marconi) with a load of 2 tnf. The composition of layer 1 was pressed with 3% of zinc stearate, which was used as a lubricating agent in the compaction.

After pressing, pure compositions (1 and 6) were sintered individually in a furnace of the Nabertherm, model Schaltplan (Nabertherm LTD, Nuremberg, Germany) at temperatures of 1000 and 1100 °C for 2 h. These tests were performed to determine whether the increment of 100 °C in sintering significantly affects the atomic diffusion of both materials, which could result in lower production costs. The limit of 1100 °C was defined according to [33,34], as the β-TCP phase becomes α-TCP in a range starting from 1125 °C up to 1430 °C. Temperatures below 1000 °C are also not appropriate for material densification. Since this temperature could not be changed, composition 1 was also submitted to a small test at 1100 °C for 4 h, to determine whether the increase in time would result in better densification (through microhardness and microscopy analysis). If 316L stainless steel presented satisfactory results for this test, it would be also applied for β-TCP. Otherwise, it would be discarded.

For all compositions, a heating rate of 10 °C/minute was applied until the material reached the sintering temperature and maintained for 2 h. Exceptionally, composition 1 and the FGM composite were submitted to a preheating of 5 °C/minute up to 400 °C for 1 h, to volatilize the zinc stearate. Inert, N5-grade argon atmosphere was used to prevent oxidation.

To evaluate the microstructure of all sintered samples, tests of laser granulometry of the Microtrac, model Turbotrac SDC (Microtrac Retsch GmbH, Pennsylvania, PA, USA) optical microscopy of the Olympus, model BX41M (Olympus CO, Tokyo, Japan), scanning electron microscopy (SEM) of the Carl Zeiss, model EVOMA 15 (Zeiss Microscopy, Jena, Germany) in the modes backscattered electrons (BSD) and mapping by energy-dispersive X-ray spectroscopy (EDS) were used.

X-ray diffraction of the PANalytical, model X'Pert Pro (Malvern Panalytical LTD, Malvern, UK) was performed on pure β-TCP after calcination and sintering, to evaluate the formed phases ($2\theta = 10^\circ$ to 90°, $0.01^\circ/s$, and followed according to the study of [35]). For the analysis of β-TCP as a powder, a cobalt tube was applied, while for β-TCP after sintering, a chromium tube was used. For the peaks to be located in the same positions,

the scan for the chrome tube was recalculated to 2θ = 20° to 100°. The software X'Pert HighScore Plus was used to identify the phases.

Archimedes' principle was employed to determine density and porosity according to ASTM C20-00 [36], as seen in Equations (2)–(4):

$$\rho_v = m/v \quad (2)$$

$$\rho_{sint} = [m/(m_{sub} - m)] * \rho_{H_2O} \quad (3)$$

$$Pa = (m_u - m/V) * 100 \quad (4)$$

where

ρ_v = green density (g/cm^3),
ρ_{sint} = sintered density (g/cm^3),
ρ_{H2O} = water density (g/cm^3),
m = dry weight (g),
m_{sub} = suspended weight (g),
m_u = saturated weight (g),
V = volume (cm^3), and
P_a = apparent porosity (%).

Mechanical properties of each sintered composition were evaluated by microhardness and compressive strength tests. For the microhardness test, a microdurometer (Time, 6301) was used, and the test was conducted according to ASTM E384-17 [37] and ASTM E92-17 [38]. The load applied was of 9.8 N, and 10 linear indentations were executed per sample. A compressive strength test has already been performed using a universal testing machine (EMIC, DL), and the test followed the ASTM E9-19 standard [39]. Stress–strain curves were obtained, and Young's modulus was determined by analyzing five points of the elastic region of each composition curve. After this, an average value was calculated according to Equation (5):

$$E = \sigma/\varepsilon \quad (5)$$

Wettability and hemocompatibility tests were performed to determine whether the powder metallurgy route generates contaminations that make 316L stainless steel/β-TCP FGM composites unfeasible to use as a biomaterial for inner implantation in the human body. The wettability test was executed in each sintered composition, using a goniometer (FM40Mk2, Krüss GmbH, Hamburg, Germany), to analyze the contact angle formed between the sessile drop and the material surface. With this, it is possible to determine the potential of body fluids to spread over the surface of sintered samples. The hemocompatibility test was accomplished to analyze the behavior of red cells when in contact with the implant surface, and it was performed in compliance with ASTM F756-17 [40]. The hemolysis rate was calculated according to Equation (6):

$$R = [(A - C_1)/C_2 - C_1)] * 100 \quad (6)$$

where

R = hemolysis rate (%),
A = sample absorbance (%),
C_1 = negative control absorbance (%), and
C_2 = positive control absorbance (%).

3. Results and Discussion

Results obtained in the tests of green and sintered density, apparent porosity, microhardness, Young's modulus, yield and ultimate compressive strength, contact angle and hemolysis rate for individual compositions and 316L/β-TCP FGM composite are presented in Table 3.

Table 3. Results obtained in the tests of green and sintered density, apparent porosity, microhardness, Young's modulus, yield and ultimate compressive strength, contact angle and hemolysis rate, performed for individual compositions and FGM composite.

	Composition		Green Density (g/cm^3)	Sintered Density (g/cm^3)	Apparent Porosity (%)	Microhardness (HV)	Young's Modulus (GPa)	Yield Strength (MPa)	Ultimate Compressive Strength (MPa)	Contact Angle (θ)	Hemolysis Rate (%)
1	**100% 316L**	1000 °C 2 h	5.46	5.92	25.28	131	1.26	115.48	126.81	-	-
		1100 °C 2 h	5.46	6.06	24.49	203	2.59	172.52	243.43	85.90	2.35
		1100 °C 4 h	-	-	-	115	-	-	-	-	-
2	**80% 316L 20% β-TCP**	-	4.53	4.85	22.12	185.17	2.27	45.86	46.24	68.73	4.47
3	**60% 316L 40% β-TCP**	-	3.76	3.98	21.58	161.80	2.08	35.98	36.23	71.30	2.62
4	**40% 316L 60% β-TCP**	-	3.01	3.28	24.59	141.50	1.87	31.28	40.44	76.00	4.08
5	**20% 316L 80% β-TCP**	-	2.54	2.83	25.68	122.20	1.73	17.18	24.81	63.33	2.42
6	**100% β-TCP**	1000 °C 2 h	2.24	2.46	27.22	43.52	1.12	10.03	10.20	-	-
		1100 °C 2 h	2.24	2.48	26.32	112.53	1.63	23.54	23.68	44.47	4.42
FGM	**-**	-	3.54	3.78	25.03	-	1.74	51.17	51.82	66.03	4.64

3.1. Evaluation of Best Sintering Temperature

To determine the best sintering temperature, pure 316L and β-TCP were evaluated at 1000 °C and 1100 °C, for 2 h. Moreover, 316L was also submitted to an additional test for 4 h (Table 3).

Analyzing the density values obtained from green to sintered samples, 316L/1000 °C showed an increase of 7.77% in densification after sintering, while 316L/1100 °C had an increase of 9.90%. From 1000 to 1100 °C, sintered 316L obtained an increase of 2.31% in density. Considering that the density of casted 316L stainless steel is 8 g/cm^3 [41], it was observed that samples sintered at 1000 °C presented 74% of densification, while those sintered at 1100 °C had 76% densification. Relating these results with those obtained by [42], who found a density of 68.7% for 1000 °C and 84.5% for 1100 °C, there is an equivalence between the values indicated in literature and those obtained in this research. Moreover, β-TCP/1000 °C presented an increase of 8.94% from green to sintered density, while β-TCP/1100 °C, an increase of 9.68%. Furthermore, from 1000 to 1100 °C, only an 0.81% increase in density was observed. Compared to the density of 3.07 g/cm^3 for β-TCP found in literature [34], the temperature of 1000 °C presented 80.13% of densification, and at 1100 °C, it was 80.78%. Mehdikhani and Borhani [43] obtained an average densification of 88% for sintered β-TCP at 1000 °C and 93% for sintered β-TCP at 1100 °C (when compared to [34]). In terms of apparent porosity, 316L/1100 °C showed values 3.13% smaller than those of 316L/1000 °C. Similarly, β-TCP/1100 °C presented an apparent porosity that was 3.31% smaller than that of β-TCP/1000 °C.

The optical microscopy results of sintered 316L stainless steel at 1000 and 1100 °C for 2 h can be seen in Figure 2, as well as at 1100 °C for 4 h. Samples treated at 1000 °C for 2 h (Figure 2a) showed well defined contours between particles. On increasing the temperature to 1100 °C for 2 h (Figure 2b), the contours became less pronounced. Keeping the temperature at 1100 °C and increasing the time to 4 h (Figure 2c), the contours remained practically the same when compared to those at 2 h. These well-defined contours between particles are due to insufficient atomic diffusion. Although there was an increase in diffusion from 1000 to 1100 °C, most of the steel reached just the first stage of sintering, with only a few particles reaching the second stage. Thus, it was verified that the increase of 100 °C in sintering was not enough to make the particles achieve a full second stage.

As observed in Figure 2, the prolongation of sintering time did not result in an improvement of atomic diffusion. Figure 3 also confirms this result, showing the grain boundaries of 316L stainless steel after sintering at 1100 °C for 2 h and 4 h. By increasing the time, the grains suffered severe growth. Particle analysis for each condition indicated an average of 130 grains/particle for 2 h, while 4 h presented an average of 14 grains/particle. A reduction of 89.23% was observed in the number of grains of particles sintered for 4 h. Comparing the grain boundaries of 316L stainless steel sintered at 1100 °C for 2 and 4 h, it was clear that the increase in sintering time worsened the microstructural conditions of 316L stainless steel, as a result of severe grain growth. It happens because of the excess of energy inserted in the process. The longer the time, the higher the tendency of grains with more energy to encompass grains with lower energy, making the total volume of contours and surface energy decrease. Thus, the propagation of cracks occurs more easily, which decreases the mechanical strength values of the material.

The bad outcome of 316L/1100 °C/4 h was also confirmed through the microhardness test (Table 3). By increasing the sintering temperature from 1000 to 1100 ° C for 2 h, microhardness increased by 35.63%. Keeping 1100 °C and changing the time to 4 h, microhardness decreased by 43.40%. In general, the condition of 1100 °C/4 h obtained the lowest microhardness between the three conditions, since the cracks moved more easily in the microstructure of 316L sintered at 4 h. Comparing the values found with literature (225 HV for casted 316L stainless steel [44]), 1000 °C/2 h presented 58.17% of the casted microhardness, while 1100 °C/2 h presented 90.39% and 1100 °C/4 h, 51.16%. After the analysis of pure 316L, the condition of 1100 °C/4 h was discarded from the compressive strength test and β-TCP analysis, due to the worse microstructural and

microhardness results that it presented. The only way to improve the atomic diffusion of 316L stainless steel would be by increasing the energy of the sintering process since both temperatures of 1000 and 1100 °C are below 1200 °C, which is indicated in literature [45] as the ideal temperature for 316L stainless steel sintering. At this temperature, the atoms of 316L achieve the third diffusional stage with only 1 h of heat treatment. However, the use of 1200 °C is not viable for 316L stainless steel/β-TCP FGM composites, due to the β-TCP → α-TCP transition at 1125 °C. The limitation in the temperature range makes the improvement of the diffusional process impossible for this steel. Thus, 1100 °C/2 h was chosen as the condition to sinter the blended compositions and the FGM composite. Although some properties showed more impressive results than others, in general, most properties presented significant improvement. This justifies the use of higher energy in the process.

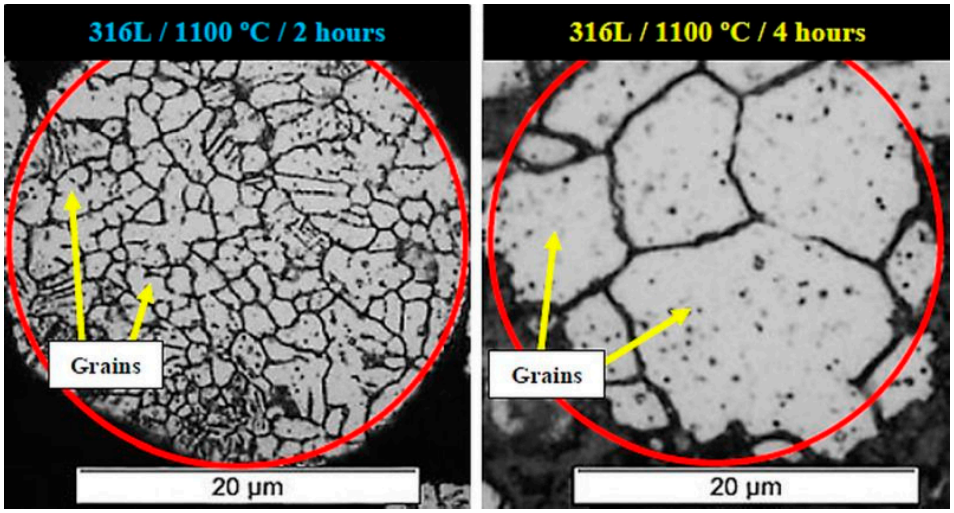


Figure 3. The 316L stainless steel particles indicating grain sizes after sintering at 1100 °C for 2 h and 4 h.

Figure 4 shows the micrographs of β-TCP sintered for 2 h at 1000 °C (Figure 4a) and 1100 °C (Figure 4b). At 1100 °C, the presence of white dots in the matrix was higher than that at 1000 °C. These dots correspond to precipitates formed during sintering.

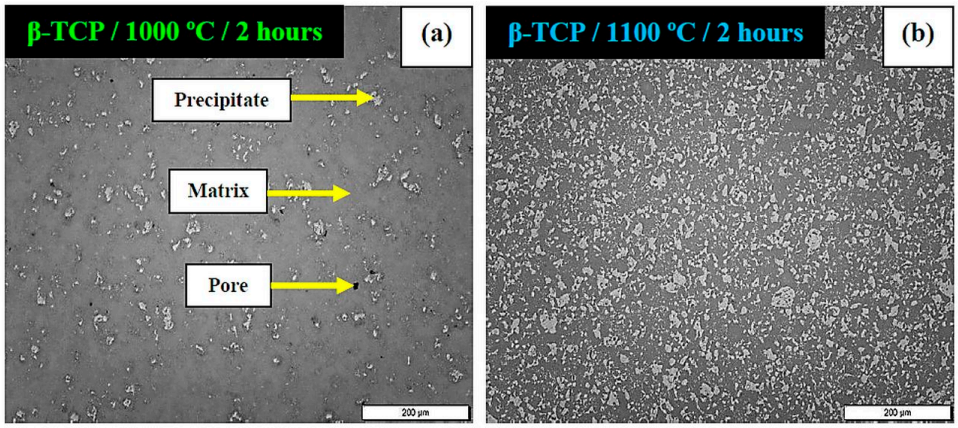


Figure 4. Micrographs of β-TCP sintered at (**a**) 1000 °C and (**b**) 1100 °C.

To determine the origin and composition of the precipitates observed in Figure 4, sintered β-TCP/1100 °C/2 h was subjected to preliminary SEM analysis (Figure 5). As seen in Figure 5a via BSD, a homogeneous matrix and the presence of pores were observed. The precipitates were not identified, as they could only be seen in optical microscopy.

Although BSD analysis did not show the location of these precipitates, surface mapping was performed to verify the possible presence of regions with different chemical compositions. As can be noted in Figure 5b, the chemical elements Ca, P, Fe and Mg, corresponding to β-TCP were homogeneously dispersed along in the matrix, showing no heterogeneity.

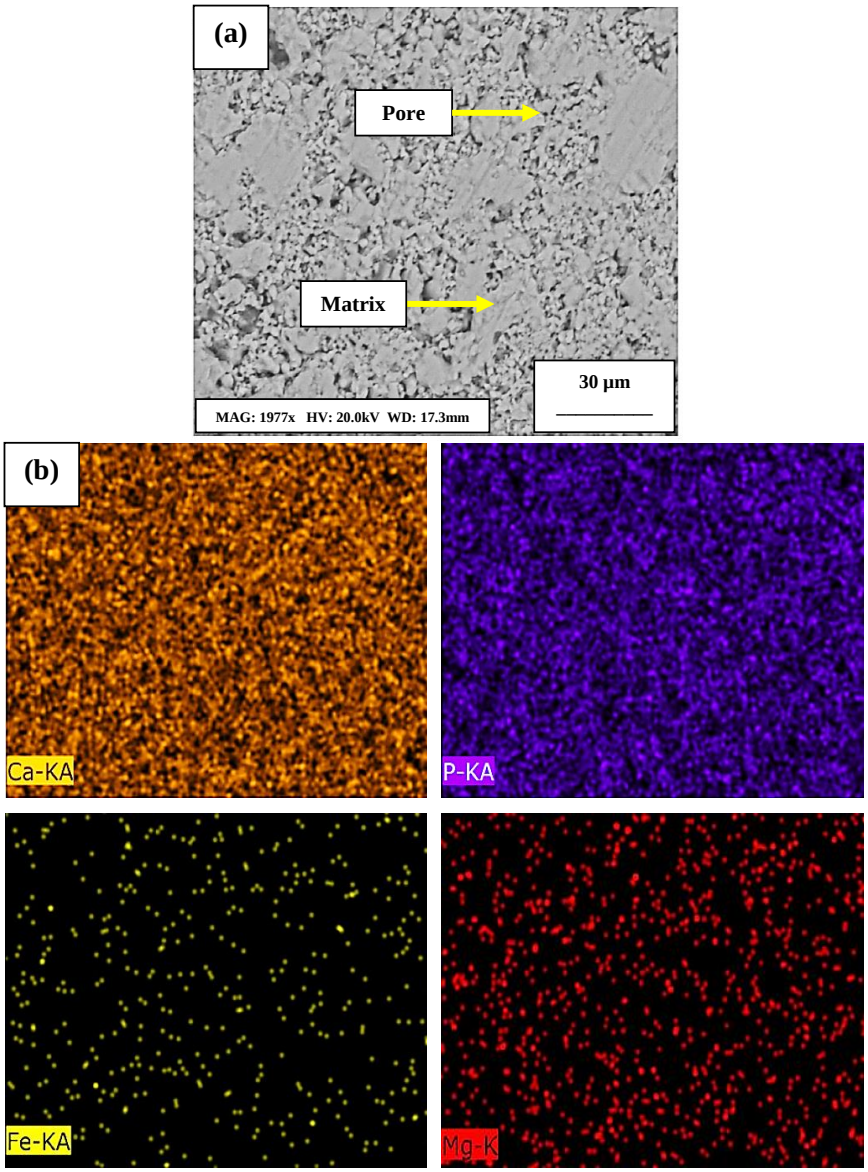


Figure 5. SEM analysis of sintered β-TCP/1100 °C/2 h: (**a**) BSD and (**b**) mapping.

Through X-ray diffraction analysis (Figure 6), it was possible to identify beyond the β-TCP phase (JCPDS 09-0169, R3c rhombohedral crystal structure), the presence of two other phases, corresponding to two calcium phosphides: CaP (JCPDS 74-0616, P62m hexagonal crystal structure) and Ca_5P_8 (JCPDS 82-0807, C2/m monoclinic crystal structure). These secondary phases corresponded to the precipitates indicated in Figure 4, formed during sintering [46]. The Ca/P system can have several crystalline phases, with the calcium phosphides CaP, Ca_3P_2 and Ca_5P_8 being the most commonly formed ones (since only a change in stoichiometry occurs). When Ca/P precipitation occurs in supersaturated aqueous solutions, a metastable amorphous phase is rapidly formed in the early stages of the reaction. After this formation, it can be converted into the most commonly found crystalline phases: hydroxyapatite ($Ca_5(PO_4)_3(OH)$), β-TCP ($Ca_3(PO_4)_2$) and pentacalcium orthophosphate (Ca_5P_8) [47,48]. These precipitates could not be observed in SEM/BSD,

being only identifiable through optical microscopy. In BSD mode, images are formed through the difference between the atomic weight of chemical elements. Since the chemical elements of matrix and precipitates are equal, no differentiation occurs in the micrographs. In optical microscopy, images are produced by light reflection. After sanding and polishing, the surface of the hardest material becomes higher (matrix or precipitate), since it resists the metallographic process more than the material with lower hardness does. Thus, optical microscopy images show different reflections between the β-TCP matrix and the precipitates formed.

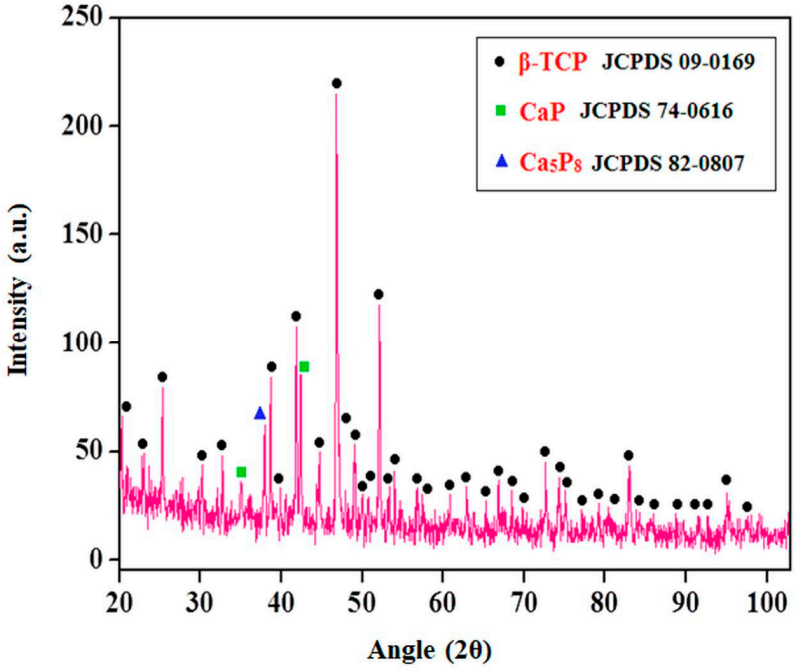


Figure 6. β-TCP diffractogram after sintering at 1100 °C for 2 h.

The microhardness test results of β-TCP sintered at 1000 and 1100 °C for 2 h can be seen in Table 3. At the temperature of 1100 °C, values 61.33% higher than those at 1000 °C were obtained. Comparing these values with those indicated by [49] for 128 HV at 1000 °C and for 229 HV at 1100 °C; sintering at 1000 °C showed 34% of this value, while at 1100 °C, it was 49.14%. Since CaP and Ca_5P_8 precipitates present greater hardness than the matrix, the better microhardness found for 1100 °C is justified by the higher presence of these precipitates for this condition, when compared to 1000 °C. The atomic diffusion was also higher with the increase of 100 °C in sintering temperature.

Stress–strain curves obtained for 316L stainless steel and β-TCP sintered at 1000 and 1100 °C/2 h are shown in Figure 7. The values obtained from these curves have already been shown in Table 3. For both temperatures, 316L stainless steel curves presented behavior consistent with literature for metallic materials, where elastic and plastic regions are clearly defined. The 316L stainless steel/1100 °C presented values of Young's modulus 51.35%, yield strength 33.06% and ultimate compressive strength 47.91% higher than those at 1000 °C. Correlating these values with those found by [42,50,51] for casted 316L stainless steel (190–200 GPa for Young's modulus, 200–700 MPa for yield strength and 330 MPa for ultimate compressive strength), the values found for both temperatures were lower: 1000 °C showed values of Young's modulus 99.34–99.37%, yield strength 42.26–83.50% and ultimate compressive strength 61.57% inferior to those in literature. In the same way, 1100 °C presented inferior values for Young's modulus (98.64–98.71%), yield strength (13.74–75.35%) and ultimate compressive strength (26.23%). Observing the Young's modulus of cortical bone (10–30 GPa) [50], the values found for 316L stainless steel

sintered at both 1000 and 1100 °C were also lower (87.4–95.8% for 1000 °C and 74.1–91.37% for 1100 °C).

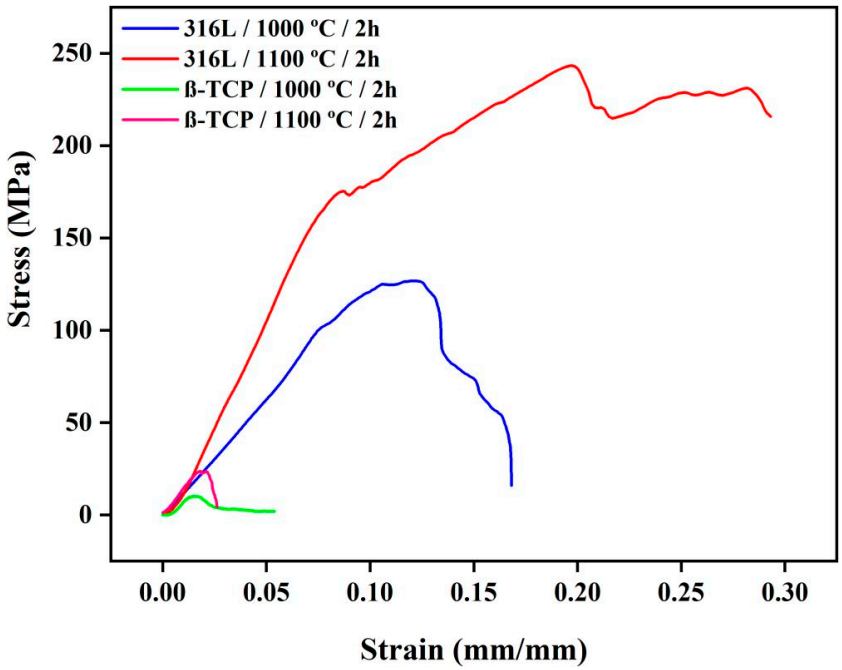


Figure 7. Stress–strain curves of 316L stainless steel and β-TCP sintered at 1000 and 1100 °C for 2 h.

Comparing β-TCP sintered at 1000 and 1100 °C with 316L stainless steel, the main difference observed in the curves of ceramic materials was the higher percentage of yield and ultimate compressive strengths that metallic materials could tolerate. While 316L supported an average stress of 100–200 MPa, β-TCP endured only 10–20 MPa. In general, from β-TCP sintered at 1000 to 1100 °C, there was an increase of 31.29% in Young's modulus, 57.39% in yield strength and 56.93% in ultimate compressive strength. Equating these values found with those indicated by [50–52] of 21 GPa for Young's modulus, 2 GPa for yield strength and 35–200 MPa for ultimate compressive strength, as well as for 316L stainless steel, β-TCP also presented values below literature. For 1000 °C, β-TCP showed values 94.67% smaller for Young's modulus, 99.50% for yield strength and 70.86–94.90% for ultimate compressive strength. Likewise, for 1100 °C, β-TCP presented values 92.24% smaller for Young's modulus, 98.82% for yield strength and 32.34–88.16% for ultimate compressive strength. Thus, both temperatures exhibited values for these properties that were below those found in the literature. In addition, the authors of [51] found a Young's modulus of 1.60 GPa for β-TCP produced with 50% of porosity. The value of 1.63 GPa obtained in this study for sintered β-TCP at 1100 °C with an apparent porosity of 26.32% was close to this value. As for 316L stainless steel, β-TCP presented, for both 1000 and 1100 °C, a Young's modulus below that of cortical bone (10–30 GPa) [50].

The results obtained in the temperature tests indicated that, for density, apparent porosity, microhardness, Young's modulus, yield and ultimate compressive strengths, both 316L stainless steel and β-TCP presented better outcomes at 1100 °C. This is due to the higher densification obtained in these samples, since an increase of 100 °C in sintering implies greater atomic diffusion, and consequently, lower porosity. Furthermore, for β-TCP, the better results found at 1100 °C are a consequence of the higher formation of CaP and Ca_5P_8 precipitates at this temperature.

In addition, materials produced by powder metallurgy naturally present reduced mechanical strength when compared to casted materials, which is attributed to the larger volume of pores that this technique provides. Pronounced porosity reduces the number of chemical bonds in the material as a whole, decreasing its mechanical strength. The larger

percentage of heterogeneous pores also results in differentiated rupture stresses between samples, making this parameter not relevant for analysis. These lower values found in mechanical properties of both 316L stainless steel and β-TCP may be inappropriate for some uses that require high strength. However, they are considered extremely important for biomaterials destined for implantation in the human body, because, when the Young's modulus of the material is higher than the Young's modulus of bone, it absorbs all tension. This absorption leads the material to experience a stress shielding effect, which leads the host bone to suffer atrophy [53].

3.2. Microstructural and Mechanical Analysis of Blended Compositions and FGM

Powder metallurgy is a process that consists of combining two or more materials through sintering to obtain a compact and uniform matrix. The green density of the compact affects strength, porosity and densification of the final material [54,55]. The properties of FGM materials obtained by powder metallurgy are also highly influenced by compaction pressure, time and temperature of sintering [56]. For these reasons, for both pure 316L stainless steel and β-TCP, green and sintered density, apparent porosity, microhardness and compressive strength tests were performed on the blended compositions and the FGM composite, after the definition of the best sintering condition (Table 3).

Each blended composition presented an increase of 5–10% from green to sintered density. Moreover, an average of a 15% decrease was observed in densities from one composition to another (2 to 5). For FGM composite, both green and sintered densities were located between the values obtained for compositions 3 and 4. Regarding apparent porosity, it was observed that as the proportion of 316L stainless steel content of compositions decreased, the apparent porosity also decreased. When a reversal between compositions 3 and 4 occurs, apparent porosity starts to rise, until it reaches a value close to pure β-TCP. The porosity of the FGM composite was located between the porosities of compositions 4 and 5. Furthermore, pure 316L stainless steel and β-TCP showed values very close to each other (24.49% and 26.32%, respectively).

For microhardness, an average pattern of a 12–14% decrease from one composition to another was observed. In the same way as for density and apparent porosity, with the decrease of 316L stainless steel content in the compositions, the values also decreased, until they reached values close to those of pure β-TCP.

Figure 8 shows the stress–strain curves of blended compositions and FGM composite. It was verified that as the percentage of β-TCP in the compositions increases, the behavior of the curves is more fragile, with an abrupt break and practically no plastic deformation. The values of yield and ultimate compressive strengths also become smaller. For compositions 3 and 4, a great similarity between both was noticed, since they have similar compositions. Curves of compositions 2 and 5 stand out from the others, as they have the highest percentages of 316L stainless steel and β-TCP among all compositions, respectively, implying a behavior more similar to the pure compositions. Composition 2 supported the highest stress among all blended compositions, while composition 5 withstood the smallest. The FGM composite presented behavior similar to that of the blended compositions and supported the second highest values of yield and ultimate compressive strengths among all individual compositions, losing just to pure 316L stainless steel (composition 1). In general, the compositions with higher content of steel presented better mechanical properties, due to the greater ductility that they possess, in comparison to ceramics.

Analyzing the values obtained for Young's modulus, yield and ultimate compressive strengths, blended compositions presented an average decrease of 5–13% in Young's modulus from one composition to another. Already for yield strength, an average decrease of 13–45% from one composition to another was noted. Lastly, for ultimate compressive strength, a variation of 10–40% was observed, of increase or decrease. The FGM composite presented values close to that of composition 5 for Young's modulus and close to those of composition 2 for yield and ultimate compressive strengths. Young's modulus is considered the most important parameter for biomaterials intended for pin, screw and plate

applications. In general, it was observed that for all compositions and the FGM composite, the values of Young's modulus were below those indicated in literature for cortical bone. Thus, the risk of bone atrophy is eliminated. However, it is necessary to evaluate the aging behavior of the composite, since the layers could be affected by the biological environment, harming the implant's performance.

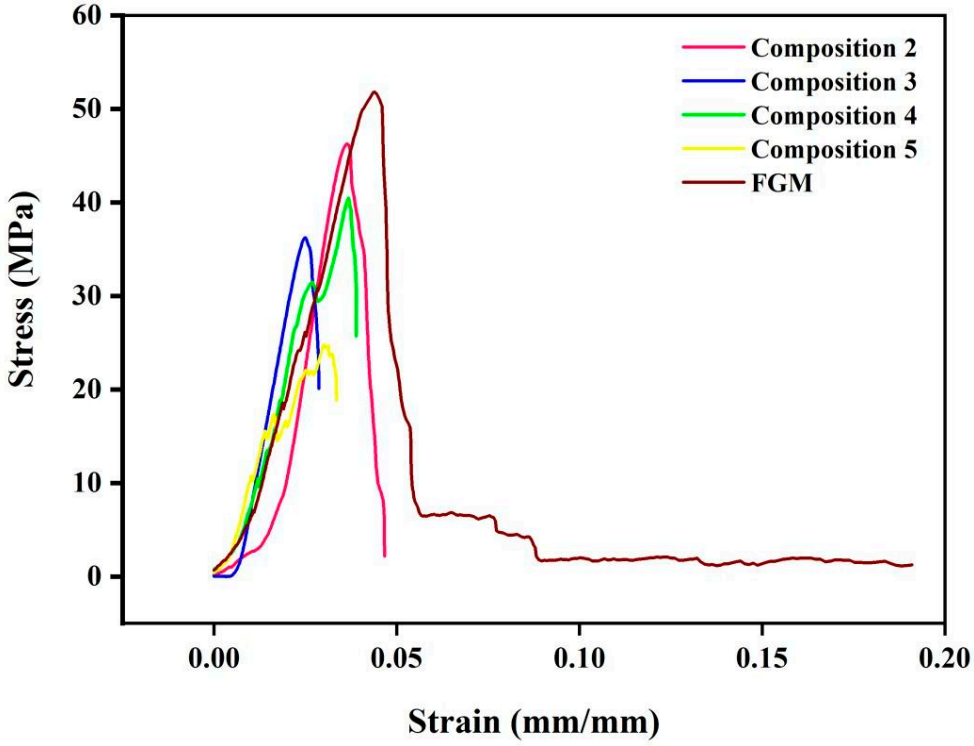


Figure 8. Stress–strain curves of blended compositions and FGM composite.

Micrographs of blended compositions can be seen in Figure 9. The 316L stainless steel particles (white regions) were homogeneously dispersed in β-TCP (dark gray regions), as well as CaP and Ca_5P_8 precipitates (light gray regions). Figure 9a (composition 2), Figure 9b (composition 3), Figure 9c (composition 4) and Figure 9d (composition 5) represent the gradual variation of the composition of the layers, where the increase in β-TCP content occurred at the same proportion by which the percentage of 316L stainless steel decreased.

The FGM composite after uniaxial pressing is shown in Figure 10. All layers were distinctly compacted on each other to form a single composite. The upper region with darker shade corresponds to 316L stainless steel, and its composition was gradually inverted until it reached the lighter shade (corresponding to β-TCP).

Optical microscopy analysis of FGM composite after sintering can be seen in Figure 11. The 316L stainless steel and β-TCP particles were homogeneously distributed along with the composite. Similarly, it was possible to evenly see the individual compositions.

Figure 12 shows SEM/EDS analysis of FGM composite by mapping. The first region of Figure 12a identifies a higher concentration of chemical elements Ca, P, and Mg, since they represent β-TCP. As the percentage of 316L stainless steel in the composite increased, the presence of Ca, P and Mg became smaller, in the same way that the chemical elements Fe, Cr, Ni, Mo, Mn and S constituents of 316L stainless steel, become higher. This was also confirmed by mapping each chemical element individually (Figure 12b).

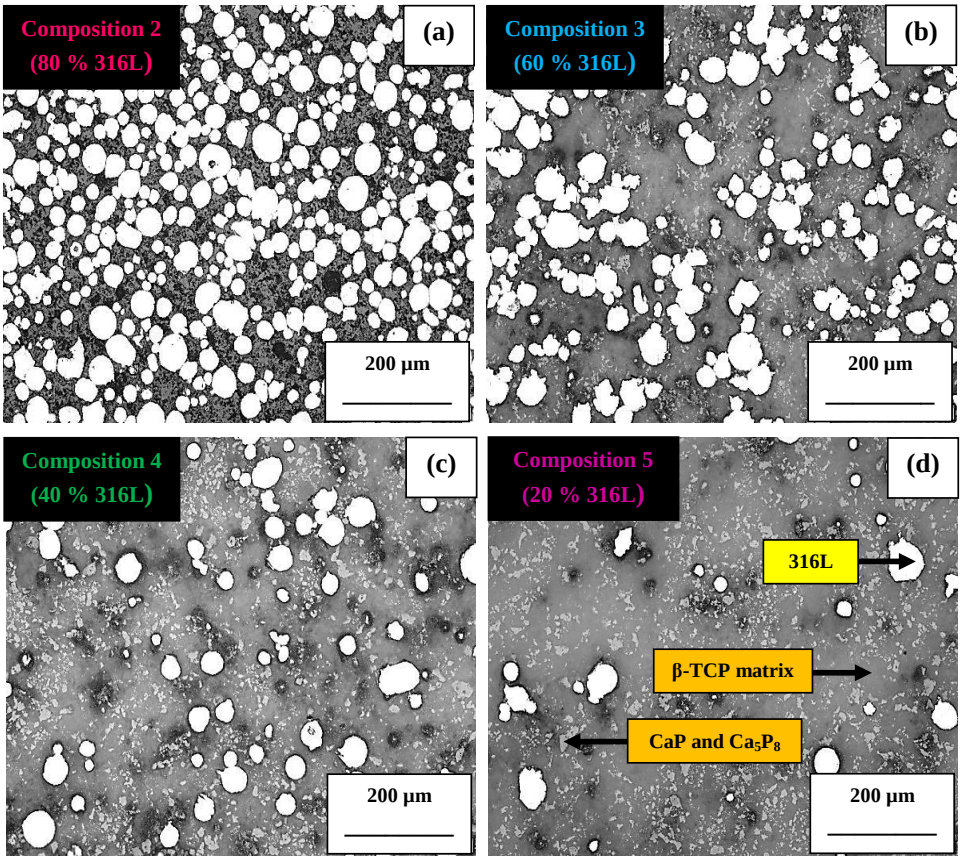


Figure 9. Micrographs of blended compositions (**a**) 2; (**b**) 3; (**c**) 4; and (**d**) 5.

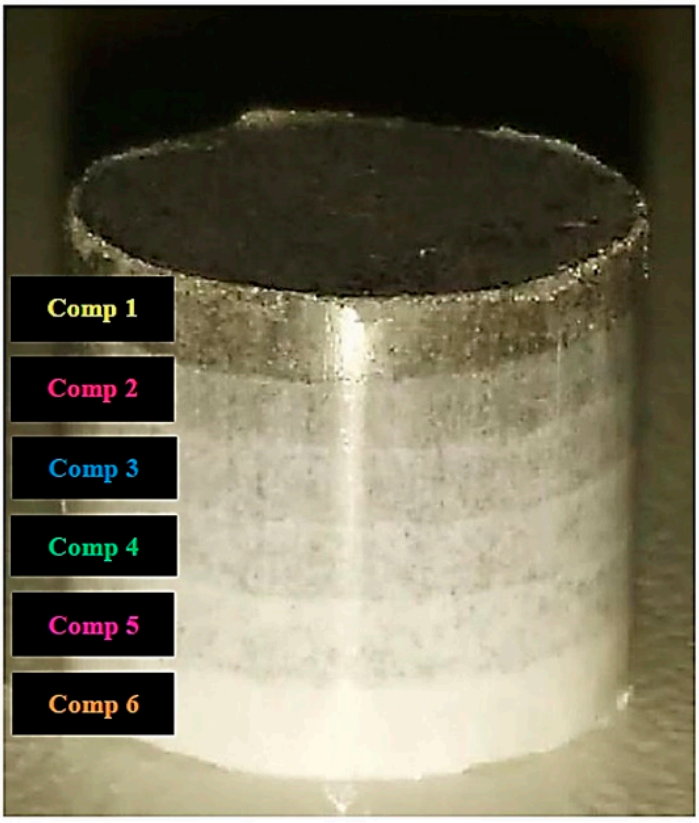


Figure 10. FGM composite after uniaxial pressing.

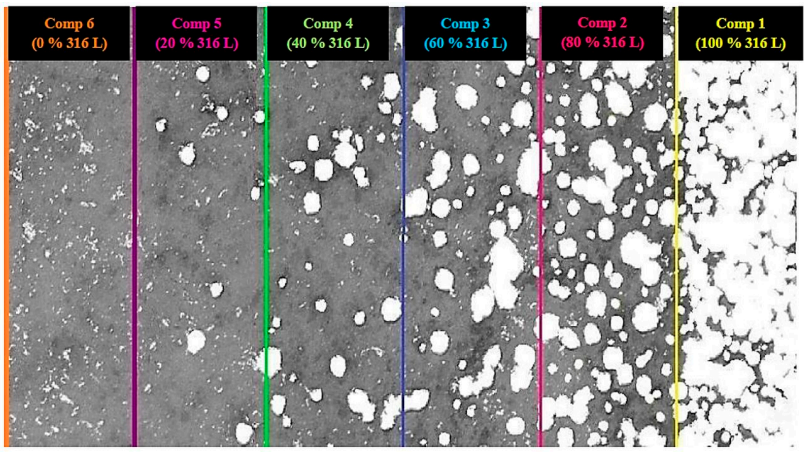


Figure 11. Optical micrographs of FGM composite.

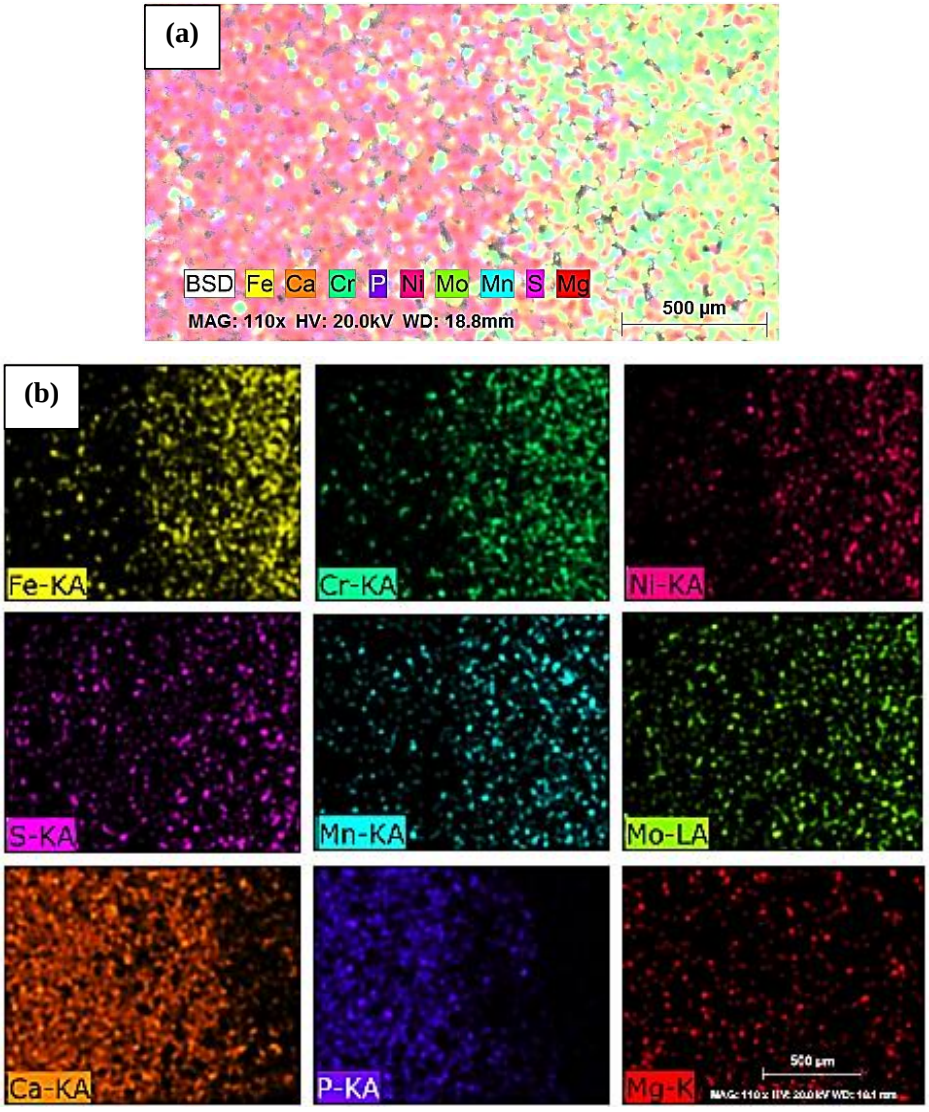


Figure 12. SEM/EDS analysis of FGM composite by mapping: (**a**) longitudinal direction and (**b**) individual chemical elements of the gradient.

Microstructural analysis of the FGM composite by optical and scanning electron microscopy showed that there was no delamination between layers, with a good interfacial bond. It indicates that the 2 tnf of load used in pressing was sufficient to properly unite the composite particles. The layers can be seen to be well defined and densified on each other, with particles of 316L stainless steel and β-TCP homogeneously distributed. It reveals that, although the diffusion of individual compositions reached only the first and second stages of sintering, it was enough to maintain the composite stable.

3.3. Wettability and Hemocompatibility Analysis of Individual Compositions and FGM

Figure 13 shows the contact angle formed between the sessile drop and the surface of the individual compositions and the FGM composite. Observing the results obtained for contact angle (Table 3), it was verified that all compositions demonstrated hydrophilic characteristics. Composition 1 showed the highest contact angle, being the closest to θ = 90° (angle that divides hydrophilic from hydrophobic behavior). Composition 6 presented the lowest contact angle. The blended compositions and the FGM composite presented angles between those of compositions 1 and 6. Composition 2, with only 20% of β-TCP, improved 20% in wettability when compared to pure 316L stainless steel. The FGM composite showed good wettability, with an angle between that of compositions 4 and 5. Comparing the results obtained with those indicated in literature for the pure materials, the values found were consistent. Metsger et al. [51] indicate a contact angle of 75° for 316L stainless steel. Similarly, Pang et al. [57] found a contact angle of 65.5° for β-TCP. Both values are very close to those found in this work. As presented in literature by [58], the larger the contact angle, the more hydrophobic the material (which tends to repel liquids from its surface). In the same way, the smaller the contact angle, the more hydrophilic the material (which tends to attract liquids to its surface). The maximum contact angle value for hydrophilic materials is θ = 90°, and above this value, the material is considered hydrophobic. For contact angle, the results showed that the addition of β-TCP significantly improved the wettability of all compositions with 316L stainless steel, due to its high hydrophilic behavior. Knowledge of hydrophobic or hydrophilic behavior is extremely important for materials intended for implants, as the more hydrophilic the material is, the greater the spreadability of body fluids over the implant surface will be and, consequently, the greater the osteointegration will be.

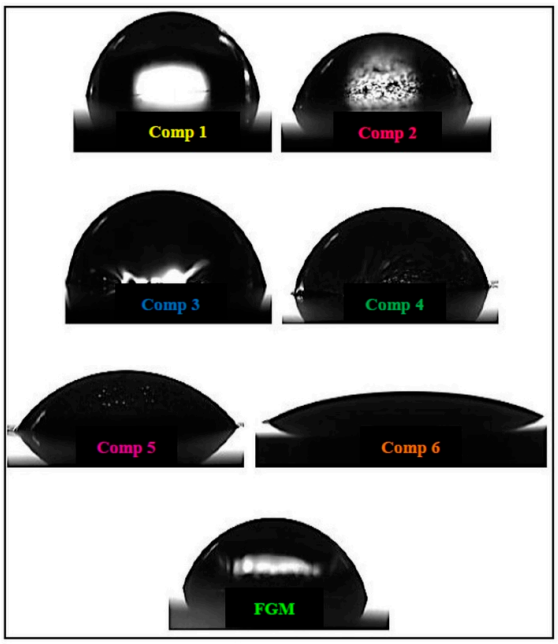


Figure 13. Contact angle formed between the sessile drop and the surface of individual compositions and FGM composite in the longitudinal direction.

Regarding hemolysis rate, it was verified in Table 3 that composition 1 was 53% below 5% of the hemolysis rate, composition 2 was 10.6%, composition 3 was 47.6%, composition 4 was 18.4%, composition 5 was 51.6%, composition 6 was 11.6% and the FGM composite was 7.2% below 5% of the hemolysis rate. Comparing the values obtained with those indicated in literature for the pure materials, there is a great consistency. For 316L stainless steel, [59] found a hemolysis rate of <3%. For β-TCP, [60] found a hemolysis rate of 2.9%. Thus, composition 1 presented a rate 53% lower than that found in literature, while β-TCP had a rate that was 34.39% higher. Even with the variability in the results presented, they are still very close and below 5% of hemolysis rate, which indicates the high hemocompatibility of the individual compositions and the FGM composite. According to ASTM F756-08 [61], materials with hemolysis up to 5% are considered highly hemocompatible. In this study, although some compositions showed slightly higher rates than others, all of them were considered highly hemocompatible, as seen in previous studies [59,62]. Even if the literature indicates that both 316L stainless steel and β-TCP have good wettability and hemocompatibility, this indication is not related to materials produced by powder metallurgy. It is known that this technique has, besides great handling (which comes from obtaining the powders, pressing and sintering), the formation of parts with a large pore volume. These factors contribute substantially to the possibility of contamination. However, as shown by [63,64], the presence of pores for biomaterials intended for implants, such as pins and bone plates, is extremely important, since the concentration of macropores interconnected with micropores increases penetration of body fluids, which improves the number of cell bonds, protein adsorption and osteogenic differentiation. Thus, despite the great inherent risk of the process, the use of porous materials is considered very advantageous, and a study of the potential for contamination is necessary. Despite this risk, both the wettability and hemocompatibility analyses performed in this research indicated that the individual compositions and the FGM composite using 316L stainless steel and β-TCP as precursor materials by powder metallurgy did not compromise their results when compared to materials produced by the conventional manufacturing processes. It is also noteworthy that the formation of CaP and Ca_5P_8 precipitates in the β-TCP matrix did not compromise its biological performance in the referred tests.

4. Conclusions

From the results obtained in this study, it was possible to conclude that

1. Tests performed to determine the ideal sintering condition indicated that the best microstructural and mechanical results were obtained for 1100 °C/2 h; the condition of 1100 °C/4 h was considered unsatisfactory.
2. The blended compositions and the FGM composite presented microstructural and mechanical properties as good as those of pure compositions (316L stainless steel and β-TCP).
3. SEM analysis of FGM composite showed good layering of each composition. Through mapping by EDS, it was observed that its chemical composition was homogeneously distributed throughout the composite.
4. For wettability and hemocompatibility tests, both individual compositions and FGM composite presented hydrophilic behavior and high hemocompatibility. It showed that 316L stainless steel/β-TCP composites produced by FGM are possible. It is because the powder metallurgy route did not insert contaminations in the composite that would make it unviable.
5. Finally, the FGM composite obtained in this study showed good microstructural and mechanical characteristics, indicating that this material could be considered as a strong candidate for dental and orthopedic applications, but additional experiments to analyze the integration between bone and implant must be performed.

Author Contributions: Conceptualization, G.S.; methodology, G.S. and B.H.B.K.; validation, B.H.B.K.; formal analysis, B.H.B.K.; investigation, B.H.B.K.; resources, D.S.; data curation, G.S.; writing—original

draft preparation, B.H.B.K. and P.C.; writing—review and editing, L.M.S.R. and P.C.; supervision and editing, D.S. and G.S.; project administration, G.S.; funding acquisition, D.S. and G.S. All authors have read and agreed to the published version of the manuscript.

Funding: This research received no external funding.

Acknowledgments: The authors would like to thank the CAPES and CNPQ and also the company Höganäs for the 316L stainless steel donation and the UNIFEI's laboratory technicians.

Conflicts of Interest: The authors declare no conflict of interest.

References

1. Mitić, Ž.; Stolić, A.; Stojanović, S.; Najman, S.; Ignjatović, N.; Nikolić, G.; Trajanović, M. Instrumental methods and techniques for structural and physicochemical characterization of biomaterials and bone tissue: A review. *Mater. Sci. Eng. C* **2017**, *79*, 930–949. [CrossRef]
2. Ghasemi-Mobarakeh, L.; Kolahreez, D.; Ramakrishna, S.; Williams, D. Key terminology in biomaterials and biocompatibility. *Curr. Opin. Biomed. Eng.* **2019**, *10*, 45–50. [CrossRef]
3. Dobrzański, L.A.; Dobrzańska-Danikiewicz, A.D.; Dobrzański, L.B. Effect of biomedical materials in the implementation of a long and healthy life policy. *Processes* **2021**, *9*, 865. [CrossRef]
4. Su, Y.; Luo, C.; Zhang, Z.; Hermawan, H.; Zhu, D.; Huang, J.; Liang, Y.; Li, G.; Ren, L. Bioinspired surface functionalization of metallic biomaterials. *J. Mech. Behav. Biomed. Mater.* **2018**, *77*, 90–105. [CrossRef]
5. Tsakiris, V.; Tardei, C.; Clicinschi, F.M. Biodegradable Mg alloys for orthopedic implants—A review. *J. Magnes. Alloy.* **2021**. [CrossRef]
6. Sivakumar, S.; Adam Khan, M.; Ebenezer, G.; Chellaganesh, D.; Vignesh, V. A review: Machinability studies on human implant materials. *Mater. Today Proc.* **2021**, *46*, 7338–7343. [CrossRef]
7. Woźniak, A.; Staszuk, M.; Reimann, Ł.; Bialas, O.; Brytan, Z.; Voinarovych, S.; Kyslytsia, O.; Kaliuzhnyi, S.; Basiaga, M.; Admiak, M. The influence of plasma-sprayed coatings on surface properties and corrosion resistance of 316L stainless steel for possible implant application. *Arch. Civ. Mech. Eng.* **2021**, *21*, 148. [CrossRef]
8. Xiao, F.; Zong, C.; Wang, W.; Liu, X.Z.; Osaka, A.; Ma, X.C. Low-temperature fabrication of titania layer on 3D-printed 316L stainless steel for enhancing biocompatibility. *Surf. Coat. Technol.* **2019**, *367*, 91–99. [CrossRef]
9. Shi, H.; Zhou, P.; Li, J.; Liu, C.; Wang, L. Functional Gradient Metallic Biomaterials: Techniques, Current Scenery, and Future Prospects in the Biomedical Field. *Front. Bioeng. Biotechnol.* **2021**, *8*, 616845. [CrossRef]
10. Essa, K.; Jamshidi, P.; Zou, J.; Attallah, M.M.; Hassanin, H. Porosity control in 316L stainless steel using cold and hot isostatic pressing. *Mater. Des.* **2018**, *138*, 21–29. [CrossRef]
11. Mehboob, H.; Chang, S.H. Evaluation of the development of tissue phenotypes: Bone fracture healing using functionally graded material composite bone plates. *Compos. Struct.* **2014**, *117*, 105–113. [CrossRef]
12. Eliaz, N.; Metoki, N. Calcium phosphate bioceramics: A review of their history, structure, properties, coating technologies and biomedical applications. *Materials* **2017**, *10*, 334. [CrossRef]
13. Cao, H.; Kuboyama, N. A biodegradable porous composite scaffold of PGA/β-TCP for bone tissue engineering. *Bone* **2010**, *46*, 386–395. [CrossRef]
14. Tanaka, T.; Komaki, H.; Chazono, M.; Kitasato, S.; Kakuta, A.; Akiyama, S.; Marumo, K. Basic research and clinical application of beta-tricalcium phosphate (β-TCP). *Morphologie* **2017**, *101*, 164–172. [CrossRef]
15. Grigoraviciute-Puroniene, I.; Tsuru, K.; Garskaite, E.; Stankeviciute, Z.; Beganskiene, A.; Ishikawa, K.; Kareiva, A. A novel wet polymeric precipitation synthesis method for monophasic β-TCP. *Adv. Powder Technol.* **2017**, *28*, 2325–2331. [CrossRef]
16. Cheng, G.; Zhang, Y.; Yin, H.; Ruan, Y.; Sun, Y.; Lin, K. Effects of Mn-doping on the structural evolution of b-Tricalcium Phosphate by Rietveld refinement and Raman spectroscopy. *Ceram. Int.* **2019**, *45*, 11073–11078. [CrossRef]
17. Hayashi, K.; Kishida, R.; Tsuchiya, A.; Ishikawa, K. Honeycomb blocks composed of carbonate apatite, β-tricalcium phosphate, and hydroxyapatite for bone regeneration: Effects of composition onbiological responses. *Mater. Today Bio* **2019**, *4*, 100031. [CrossRef]
18. Carson, J.S.; Bostrom, M.P.G. Synthetic bone scaffolds and fracture repair. *Injury* **2007**, *38*, S33–S37. [CrossRef]
19. Seo, J.Y.; Lee, K.Y.; Shim, D.S. Effects of process parameters on properties of porous foams formed by laser-assisted melting of steel powder (AISI P21)/foaming agent (ZrH2) mixture. *Opt. Laser Technol.* **2018**, *98*, 326–338. [CrossRef]
20. Sikora-Jasinska, M.; Paternoster, C.; Mostaed, E.; Tolouei, R.; Casati, R.; Vedani, M.; Mantovani, D. Synthesis, mechanical properties and corrosion behavior of powder metallurgy processed Fe/Mg2Si composites for biodegradable implant applications. *Mater. Sci. Eng. C* **2017**, *81*, 511–521. [CrossRef]
21. Salimi, E. Functionally graded calcium phosphate bioceramics: An overview of preparation and properties. *Ceram. Int.* **2020**, *46*, 19664–19668. [CrossRef]
22. Deng, J.; Liu, Y.; Zhang, Z.; Liu, W. Size-dependent vibration and stability of multi-span viscoelastic functionally graded material nanopipes conveying fluid using a hybrid method. *Compos. Struct.* **2017**, *179*, 590–600. [CrossRef]

23. Höganäs AB. *Datasheet: 3045HOG 316L Austenitic Stainless Steel for Laser Powder Bed Fusion*; Höganäs AB: Hoganas, Sweden, 2020; pp. 2–3. Available online: https://www.hoganas.com/globalassets/download-media/sharepoint/brochures-and-datasheets---all-documents/additeve-manufacturing_am-316l_20-53_3045hog.pdf (accessed on 10 January 2021).
24. Almeida, J.A.M.; Kuffner, B.H.B.; Silva, G.; Capellato, P.; Sachs, D. Analysis of the influence of β-TCP particle size on deagglomeration processes. *Res. Soc. Dev.* **2020**, *9*, e175943067. [CrossRef]
25. Feng, D.; Feng, Y.; Yuan, S.; Zhang, X.; Wang, G. Melting behavior of Ag nanoparticles and their clusters. *Appl. Therm. Eng.* **2017**, *111*, 1457–1463. [CrossRef]
26. Kowsar, S.; Soheilifard, R. The effect of the degradation pattern of biodegradable bone plates on the healing process using a biphasic mechano-regulation theory. *Biomech. Model. Mechanobiol.* **2021**, *20*, 309–321. [CrossRef]
27. Mehboob, H.; Chang, S.H. Optimal design of a functionally graded biodegradable composite bone plate by using the Taguchi method and finite element analysis. *Compos. Struct.* **2015**, *119*, 166–173. [CrossRef]
28. Salavati, H.; Mohammadi, H.; Yusefi, A.; Berto, F. Fracture assessment of V-notched specimens with end holes made of tungsten-copper functionally graded material under mode I loading. *Theor. Appl. Fract. Mech.* **2018**, *97*, 357–367. [CrossRef]
29. Mohammadi, H.; Salavati, H.; Alizadeh, Y.; Berto, F. Prevalent mode II fracture assessment of inclined U-notched specimens made of tungsten-copper functionally graded material. *Theor. Appl. Fract. Mech.* **2017**, *89*, 90–99. [CrossRef]
30. Valarezo, A.; Bolelli, G.; Choi, W.B.; Sampath, S.; Cannillo, V.; Lusvarghi, L.; Rosa, R. Damage tolerant functionally graded WC-Co/Stainless Steel HVOF coatings. *Surf. Coat. Technol.* **2010**, *205*, 2197–2208. [CrossRef]
31. Thomas, G.; Vincent, R.; Matthews, G.; Dance, B.; Grant, P.S. Interface topography and residual stress distributions in W coatings for fusion armour applications. *Mater. Sci. Eng. A* **2008**, *477*, 35–42. [CrossRef]
32. Lin, X.; Yue, T.M. Phase formation and microstructure evolution in laser rapid forming of graded SS316L/Rene88DT alloy. *Mater. Sci. Eng. A* **2005**, *402*, 294–306. [CrossRef]
33. Torres, P.; Abrantes, J.; Kaushal, A.; Pina, S.; Dobelin, N.; Bohner, M.; Ferreira, J. Influence of Mg-doping, calcium pyrophosphate impurities and cooling rate on the allotropic α ↔ β-tricalcium phosphate phase transformations. *J. Eur. Ceram. Soc. J.* **2015**, *36*, 817–827. [CrossRef]
34. Carrodeguas, R.G.; De Aza, S. α-Tricalcium phosphate: Synthesis, properties and biomedical applications. *Acta Biomater.* **2011**, *7*, 3536–3546. [CrossRef]
35. Cardoso, H.A.I.; Motisuke, M.; Zavaglia, C.A.C. Analysis of the influence of two different milling processes on the properties of beta-TCP precursor powder and cement. *Ceramica* **2012**, *58*, 225–228. [CrossRef]
36. ASTM International. *ASTM C20-00: Standard Test Methods for Apparent Porosity, Water Absorption, Apparent Specific Gravity, and Bulk Density of Burned Refractory Brick and Shapes by Boiling Water*; ASTM International: West Conshohocken, PA, USA, 2010; Volume 15.01, pp. 1–3. [CrossRef]
37. ASTM International. ASTM E384: Standard Test Method for Microindentation Hardness of Materials. In *American Society for Testing Materials Handbook*; ASTM International: West Conshohocken, PA, USA, 2017; Volume 03.01, pp. 281–293. [CrossRef]
38. ASTM International. *ASTM E92-17: Standard Test Methods for Vickers Hardness and Knoop Hardness of Metallic Materials BT—Standard Test Methods for Vickers Hardness and Knoop Hardness of Metallic Materials*; ASTM International: West Conshohocken, PA, USA, 2017; Volume 03.01, pp. 1–27. [CrossRef]
39. ASTM International. *ASTM E9-19: Standard Test Methods of Compression Testing of Metallic Materials at Room Temperature*; ASTM International: West Conshohocken, PA, USA, 2019; Volume 03.01, pp. 1–9. [CrossRef]
40. ASTM International. *ASTM F756-17: Standard Practice for Assessment of Hemolytic Properties of Materials*; ASTM International: West Conshohocken, PA, USA, 2017; Volume 13.01, p. 5. [CrossRef]
41. Nasr, M.N.A.; Ng, E.G.; Elbestawi, M.A. Modelling the effects of tool-edge radius on residual stresses when orthogonal cutting AISI 316L. *Int. J. Mach. Tools Manuf.* **2007**, *47*, 401–411. [CrossRef]
42. Choi, J.P.; Lee, G.Y.; Song, J.-I.; Lee, W.S.; Lee, J.S. Sintering behavior of 316L stainless steel micro-nanopowder compact fabricated by powder injection molding. *Powder Technol.* **2015**, *279*, 196–202. [CrossRef]
43. Mehdikhani, B.; Borhani, G.H. Densification and Mechanical Behavior of β-Tricalcium Phosphate Bioceramics. *Int. Lett. Chem. Phys. Astron.* **2014**, *36*, 37–49. [CrossRef]
44. Ziętala, M.; Durejko, T.; Polański, M.; Kunce, I.; Płociński, T.; Zieliński, W.; Łazińska, M.; Stępniowski, W.; Czujko, T.; Kurzydłowski, K.J.; et al. The microstructure, mechanical properties and corrosion resistance of 316L stainless steel fabricated using laser engineered net shaping. *Mater. Sci. Eng. A* **2016**, *677*, 1–10. [CrossRef]
45. Cao, M.; Jiang, F.; Wang, C.; Cui, H.; Guo, C.; Chang, Y.; Wang, Z. Preparation, microstructure and mechanical property of double-layered metal-ceramic hollow spheres. *Mater. Sci. Eng. A* **2020**, *780*, 139188. [CrossRef]
46. Singh, R.P.; Batra, U. Structure and properties of silver-doped calcium phosphate nanopowders. *Bull. Mater. Sci.* **2016**, *39*, 1285–1294. [CrossRef]
47. Kostov-Kytin, V.V.; Dyulgerova, E.; Ilieva, R.; Petkova, V. Powder X-ray diffraction studies of hydroxyapatite and β-TCP mixtures processed by high energy dry milling. *Ceram. Int.* **2018**, *44*, 8664–8671. [CrossRef]
48. Nascimento, R.M.; Faita, F.L.; Agostini, D.L.S.; Job, A.E.; Guimarães, F.E.G.; Bechtold, I.H. Production and characterization of natural rubber-Ca/P blends for biomedical purposes. *Mater. Sci. Eng. C* **2014**, *39*, 29–34. [CrossRef]
49. Amanov, A.; Lee, S.W.; Pyun, Y.S. Low friction and high strength of 316L stainless steel tubing for biomedical applications. *Mater. Sci. Eng. C* **2017**, *71*, 176–185. [CrossRef]

50. Chen, Q.; Thouas, G.A. Metallic implant biomaterials. *Mater. Sci. Eng. R Rep.* **2015**, *87*, 1–57. [CrossRef]
51. Metsger, D.S.; Rieger, M.R.; Foreman, D.W. Mechanical properties of sintered hydroxyapatite and tricalcium phosphate ceramic. *J. Mater. Sci. Mater. Med.* **1999**, *10*, 9–17. [CrossRef]
52. Chicot, D.; Tricoteaux, A.; Lesage, J.; Leriche, A.; Descamps, M.; Rguiti-Constantin, E. Mechanical Properties of Porosity-Free Beta Tricalcium Phosphate (β-TCP) Ceramic by Sharp and Spherical Indentations. *New J. Glas. Ceram.* **2013**, *03*, 16–28. [CrossRef]
53. Pillar, R.M. Metallic Biomaterials. In *Biomedical Materials*; Narayan, R., Ed.; Springer: Toronto, ON, Canada, 2021; pp. 1–48. ISBN 9783030492052.
54. Marzuki, M.; Mazni Ismail, N.; Ihsan Abdul Latiff, M. Preparation and Microstructural Characterization of Five-layered Aluminium-Aluminium Oxide Functionally Graded Material. *IOP Conf. Ser. Mater. Sci. Eng.* **2021**, *1092*, 012031. [CrossRef]
55. Al-Qureshi, H.A.; Soares, M.R.F.; Hotza, D.; Alves, M.C.; Klein, A.N. Analyses of the fundamental parameters of cold die compaction of powder metallurgy. *J. Mater. Process. Technol.* **2008**, *199*, 417–424. [CrossRef]
56. Pasha, A.; Rajaprakash, B.M. Fabrication and mechanical properties of functionally graded materials: A review. *Mater. Today Proc.* **2021**. [CrossRef]
57. Pang, D.; He, L.; Wei, L.; Zheng, H.; Deng, C. Preparation of a beta-tricalcium phosphate nanocoating and its protein adsorption behaviour by quartz crystal microbalance with dissipation technique. *Colloids Surf. B Biointerfaces* **2018**, *162*, 1–7. [CrossRef]
58. Menzies, K.L.; Jones, L. The impact of contact angle on the biocompatibility of biomaterials. *Optom. Vis. Sci.* **2010**, *87*, 387–399. [CrossRef]
59. Shang, Y.; Yuan, Y.; Li, D.; Li, Y.; Chen, J. Effects of scanning speed on in vitro biocompatibility of 316L stainless steel parts elaborated by selective laser melting. *Int. J. Adv. Manuf. Technol.* **2017**, *92*, 4379–4385. [CrossRef]
60. Krishna Samanta, S.; Chanda, A. Study on the Structure and Properties of Crystalline Pure and Doped β-Tri Calcium Phosphate Ceramics. *Mater. Today Proc.* **2018**, *5*, 2330–2338. [CrossRef]
61. ASTM International. *ASTM F 756-00: Standard Practice for Assessment of Hemolytic Properties of Materials*; ASTM International: West Conshohocken, PA, USA, 2000; Volume 13.01, p. 5.
62. Esmaeili, A.; Ghaffari, S.A.; Nikkhah, M.; Malek Ghaini, F.; Farzan, F.; Mohammadi, S. Biocompatibility assessments of 316L stainless steel substrates coated by Fe-based bulk metallic glass through electro-spark deposition method. *Colloids Surf. B Biointerfaces* **2021**, *198*, 111469. [CrossRef]
63. Mihalcea, E.; Vergara-Hernández, H.J.; Jimenez, O.; Olmos, L.; Chávez, J.; Arteaga, D. Design and characterization of Ti6Al4V/20CoCrMo−highly porous Ti6Al4V biomedical bilayer processed by powder metallurgy. *Trans. Nonferrous Met. Soc. China (Engl. Ed.)* **2021**, *31*, 178–192. [CrossRef]
64. Sharma, A.; Mishra, P. Microstructure and mechanical behaviour of Ti-Cu foams synthesized via powder metallurgy technique. *Mater. Res. Express* **2021**, *8*, 035402. [CrossRef]